

# Role of intermediate resonances in attosecond photoelectron interferometry in neon

M. Moioli<sup>1</sup>, M. M. Popova, K. R. Hamilton<sup>2,3</sup>, D. Ertel<sup>1</sup>, D. Busto<sup>1,4</sup>, I. Makos<sup>1</sup>,  
M. D. Kiselev, S. N. Yudin, H. Ahmadi<sup>1</sup>, C. D. Schröter<sup>5</sup>, T. Pfeifer<sup>5</sup>, R. Moshhammer<sup>5</sup>,  
E. V. Gryzlova, A. N. Grum-Grzhimailo, K. Bartschat<sup>2</sup>, and G. Sansone<sup>1,\*</sup>

<sup>1</sup> *Physics Department University of Freiburg, Freiburg 79014, Germany*

<sup>2</sup> *Department of Physics and Astronomy, Drake University, Des Moines, Iowa 50311, USA*

<sup>3</sup> *Department of Physics, University of Colorado Denver, Denver, Colorado 80204, USA*

<sup>4</sup> *Department of Physics, Lund University, SE-221 00 Lund, Sweden and*

<sup>5</sup> *Max-Planck-Institut für Kernphysik, 69117 Heidelberg, Germany.\**

(Dated: October 8, 2024)

Attosecond photoelectron interferometry based on the combination of an attosecond pulse train and a synchronized infrared field is a fundamental technique for the temporal characterization of attosecond waveforms and for the investigation of electron dynamics in the photoionization process. In this approach, the comb of extreme ultraviolet harmonics typically lies above the ionization threshold of the target under investigation, thus releasing a photoelectron by single-photon absorption. The interaction of the outgoing photoelectron with the infrared pulse results in the absorption or emission of infrared photons, thereby creating additional peaks in the photoelectron spectrum, referred to as sidebands. While, in the absence of resonances in the first ionization step, the phases imparted on the photoionization process evolve smoothly with the photon energy, the presence of intermediate resonances imprints a large additional phase on the outgoing photoelectron wave packet. In this work, using a comb of harmonics below and above the ionization threshold of neon, we investigate the effect of intermediate bound excited states on attosecond photoelectron interferometry. We show that the phase of the oscillations of the sidebands and their angular distributions are strongly affected by such resonances. By slightly tuning the photon energies of the extreme ultraviolet harmonics, we show how the contributions of selected resonances can be enhanced or suppressed.

## I. INTRODUCTION

The reconstruction of attosecond beating by interference of two-photon transitions (RABBIT) technique was demonstrated in 2001 [1], with the goal to reconstruct the temporal profile of an attosecond pulse train. The oscillations in the photoelectron spectra for the two-color photoionization process as a function of the relative delay  $\tau$  between the extreme ultraviolet (XUV) and infrared (IR) pulses contain information about the phase difference between consecutive harmonics, thereby giving access to the attosecond chirp [2, 3]. This information can be extracted from the experimental data, provided that the target-specific phases imprinted on the photoelectron wave packets are known and can be subtracted from the measured phase differences. In the case of XUV photon energies well above the ionization threshold, and in the absence of resonances in the continuum, these phases are expected to evolve smoothly with the photon energy. In atoms, they can be further decomposed into a photoionization phase, associated with the photoionization process due to the absorption of a single XUV photon, and a continuum-continuum phase due to the interaction of the outgoing photoelectron wave packet with the IR field [4–6]. More recently, the validity of this “decomposition approximation” was generalized and tested also for multiple continuum-continuum transitions [7–9].

The presence of intermediate resonances, however, either in the continuum or in the bound-state spectral region, is expected to play a crucial role in attosecond photoelectron interferometry, as these levels can modify the amplitude and phase of one or even both of the two pathways contributing to the interference signal [10]. These effects have been investigated in helium, addressing the role of intermediate bound states reached by single XUV-photon ionization [11–14] and of doubly-excited states in the continuum [15]. In helium, the large energetic distance between consecutive excited levels accessible by single-photon excitation from the ground state, compared to the width of a single harmonic, makes it possible to address individual resonances for each configuration of the harmonics.

In heavier noble-gas atoms on the other hand, the manifold of excited states accessible by dipole transitions from the ground state becomes energetically closer [16]. A single harmonic may thus excite more than one level, thereby generating a rich interference structure in the photoelectron signal in the continuum. Recently, the effect of an intermediate resonance in the interference between two pathways determined by XUV colors was also investigated [17, 18]. In molecules, intermediate shape resonances can also affect the phase of the photoemission measured in the laboratory [19] and in the recoil frame [20, 21] of the target system.

The scheme of the present study is presented in Fig. 1. A comb of XUV harmonics generated by high-order harmonic generation (HHG) in gases includes harmonics below (harmonic  $2q - 3$ ) and above (harmonics  $2q - 1$  and  $2q + 1$ ) the ionization threshold of neon. While the

---

\* corresponding author: [giuseppe.sansone@physik.uni-freiburg.de](mailto:giuseppe.sansone@physik.uni-freiburg.de)

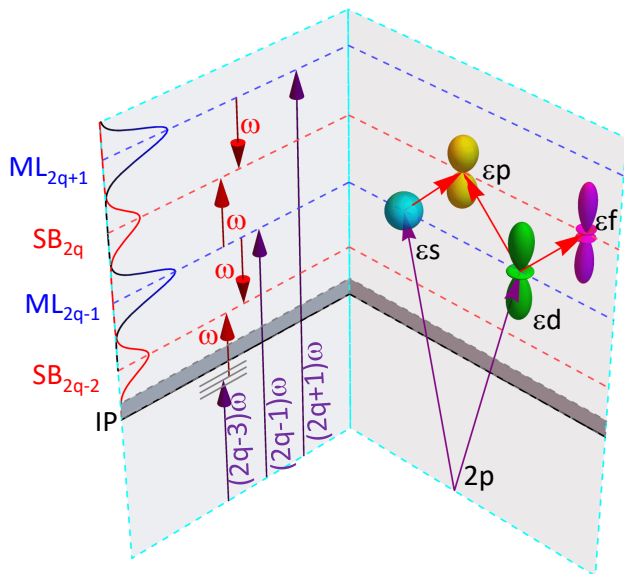


FIG. 1. Scheme of the energy levels and angular character of the photoelectron wave packets emitted by a comb of odd XUV harmonics around the ionization threshold of neon. The UT-RABBIT mechanism is formed by the harmonics  $2q - 3$  and  $2q - 1$ , while the pairs  $2q - 1$  and  $2q + 1$  form the AT-RABBIT  $SB_{2q}$  line. The angular distributions on the right-hand-side describe schematically the photoelectron with kinetic energy  $\epsilon$  in the continuum. These electrons are ejected after absorption of a single XUV photon, resulting in  $\epsilon s$  and  $\epsilon d$  states. Their partial-wave character is then further modified by the absorption (or emission) of an additional IR photon, resulting in  $\epsilon p$  and  $\epsilon f$  states.

harmonic below the ionization threshold can populate a resonant bound excited state, the absorption of a single XUV photon above the ionization threshold leads to the direct emission of a photoelectron (indicated as main lines  $ML_{2q-1}$  and  $ML_{2q+1}$ ). As a consequence, the first sideband above the ionization threshold ( $SB_{2q-2}$ ) is formed by the interference of one path influenced by the presence of a manifold of bound states below the ionization threshold and another one resulting from non-resonant ionization above the ionization threshold. We label the process leading to the formation of the sideband  $S_{2q-2}$  as “under-threshold” (UT)-RABBIT [10, 22], because of the involvement of the bound state below the ionization threshold. In contrast, the “above-threshold” (AT)-RABBIT mechanism occurs when both XUV absorption processes already lead to the continuum.

The absorption of a single XUV photon resulting in an electron ejected from the  $2p$  subshell of neon leads to the population of continuum states with  $s$  and  $d$  character, i.e., orbital angular momenta  $\ell = 0$  and  $\ell = 2$ , respectively [23]. The subsequent absorption or emission of an IR photon will result in population of final states with  $p$  ( $\ell = 1$ ) and  $f$  ( $\ell = 3$ ) character. The right-hand-side of Fig. 1 shows schematically the character of the different states populated by the absorption of an XUV and IR photon above the ionization threshold of neon.

The same conclusions are valid when the first XUV photon populates a bound state below the ionization threshold.

## II. EXPERIMENTAL SETUP

The experimental campaigns were performed using two experimental attosecond sources described in detail in refs. [24, 25]. For the first one, the laser driving the HHG was a titanium-doped sapphire system operating at 10 kHz, with a central wavelength of  $\lambda = 800$  nm delivering pulses with an energy of 1 mJ and a duration (FWHM of intensity profile) of 30 fs. The second one produced IR pulses starting from a Yb:KGW regenerative amplifier with a central wavelength of 1025 nm, 50 kHz repetition rate, and 400  $\mu$ J pulse energy. The original pulse duration of 277 fs was reduced to 17.8 fs by exploiting nonlinear broadening in a gas-filled hollow-core fiber (HCF) and subsequent temporal compression using chirped mirrors. [25]. In the HCF, the type and the pressure of the gas lead to different blue shifts of the central wavelength, thereby offering the possibility to slightly tune the central wavelength in the range between 1001 nm and 1019 nm with an uncertainty of about  $\pm 5$  nm.

In both beamlines, a delay between the IR pulses and the XUV attosecond pulse train was introduced and controlled with an ultra-stable collinear setup based on drilled glass plates [24, 25].

The XUV and IR pulses were focused by a toroidal mirror in a 3D-momentum-imaging spectrometer (reaction microscope) [26], where they interacted with a supersonic neon gas jet. The products of the ionization were then guided to the photoelectron and photoion detectors by suitable electric and magnetic fields. Here, the peak intensities of the IR pulses at the interaction region of the reaction microscope were estimated as  $I_{\text{IR}} \approx 1 \times 10^{12}$  W/cm<sup>2</sup> and  $I_{\text{IR}} \approx 7 \times 10^{11}$  W/cm<sup>2</sup> for the first and second experimental setup, respectively. At the same position, the highest peak intensity of a single attosecond pulse in the train for the two setups was  $I_{\text{XUV}} \approx 2 \times 10^{10}$  W/cm<sup>2</sup> and  $I_{\text{XUV}} \approx 5 \times 10^9$  W/cm<sup>2</sup>, respectively.

The spectral distribution of the XUV harmonics was characterized using an XUV spectrometer placed after the coincidence spectrometer. The duration of each harmonic was estimated as  $\approx 9$  fs for 800 nm and  $\approx 6$  fs for 1006 nm by considering the width of the corresponding spectral peaks, the XUV spectrometer resolution, and assuming a gaussian envelope.

The experimental parameters for the IR and XUV fields used in our experiments are summarized in Table I. The strength of the electric field of each harmonic is given relative to the 19<sup>th</sup> harmonic for 800 nm and the 25<sup>th</sup> harmonic for 1006 nm, respectively. The lowest (11<sup>th</sup> for 800 nm and 13<sup>th</sup>-15<sup>th</sup> for 1006 nm) and the highest (23<sup>rd</sup> for 800 nm and 31<sup>st</sup> for 1006 nm) harmonics were outside the spectral range of the XUV spectrometer.

Their intensities are assumed to be equal to the closest harmonic measured in the experiment. The phases of the lowest harmonics (including those contributing to the UT-RABBIT) and highest harmonics were determined assuming a constant value of the group delay dispersion (GDD) determined from the oscillations of the closest AT-RABBIT sidebands.

We consider the RABBIT scheme for the angle-integrated electron emission probability as well as photoelectron angular distributions (PADs):

$$S(\theta, \tau) = S_0(\theta) + S_2(\theta) \cos(2\omega_{\text{IR}}\tau - \phi(\theta)). \quad (1)$$

Here,  $\theta$ ,  $\omega_{\text{IR}}$ , and  $\tau$  indicate the ejected-electron angle defined with respect to the polarization axis of the fields, the frequency of the IR field, and the relative delay between the attosecond pulse train and the IR field, respectively. The phase  $\phi(\theta)$  is the phase introduced by the photoionization process, which, in general, depends on the emission angle of the photoelectron. By averaging the delays  $\tau$  over an integer number of periods  $T$  of the IR, the PAD can be described using the angular anisotropy parameters  $\beta_n$  and the Legendre polynomials  $P_n$  according to the formula:

$$S_0(\theta) = \frac{S_0}{4\pi} [1 + \beta_2 P_2(\cos \theta) + \beta_4 P_4(\cos \theta)]. \quad (2)$$

Integrating Eq. (1) over the angles yields

$$S_0(\tau) = S_0 + S_2 \cos(2\omega_{\text{IR}}\tau - \phi). \quad (3)$$

In addition to the  $(\theta, \tau)$  dependence written explicitly, all observable values are functions of the photoelectron energy  $\varepsilon$ , which is omitted for brevity of notation.

TABLE I. Parameters of the polychromatic XUV field. The error values of the amplitudes  $E_{2q+1}$  are calculated as the standard deviation of the average values around each harmonic maxima. For the phases  $\phi_{2q+1}$ , the error values are evaluated by weighting the standard deviation of the phases around the harmonic maxima with the corresponding amplitude values around the peak.

	Harmonic order $2q+1$	$E_{2q+1}$	$\phi_{2q+1}$ (rad)
$\lambda = 800$ nm	11	$0.37 \pm 0.02$	$0.00 \pm 0.02$
	13	$0.37 \pm 0.02$	$0.79 \pm 0.02$
	15	$0.68 \pm 0.01$	$-1.93 \pm 0.02$
	17	$0.93 \pm 0.01$	$-3.46 \pm 0.02$
	19	$1.00 \pm 0.01$	$0.85 \pm 0.07$
	21	$0.82 \pm 0.01$	$-1.51 \pm 0.39$
	23	$0.82 \pm 0.01$	$-4.13 \pm 0.39$
$\lambda = 1006$ nm	13	$0.59 \pm 0.01$	$0.00 \pm 0.01$
	15	$0.59 \pm 0.01$	$0.04 \pm 0.01$
	17	$0.59 \pm 0.01$	$-0.23 \pm 0.01$
	19	$0.86 \pm 0.02$	$-0.78 \pm 0.05$
	21	$0.97 \pm 0.01$	$-1.63 \pm 0.03$
	23	$0.92 \pm 0.02$	$-2.72 \pm 0.08$
	25	$1.00 \pm 0.01$	$2.23 \pm 0.03$
	27	$0.99 \pm 0.01$	$0.48 \pm 0.07$
	29	$0.85 \pm 0.01$	$-1.56 \pm 0.1$
	31	$0.85 \pm 0.01$	$2.39 \pm 0.1$

Both the RABBIT phase and the  $\beta_n$  parameters can be extracted by fitting experimental data and theoretical predictions to the above forms.

### III. THEORETICAL MODELS

In this section, we summarize the theoretical models used to predict the observables of interest. They are:

- the nonrelativistic R-matrix with time dependence (RMT) approach,
- a relativistic time-dependent perturbation theory (PT), and
- an approach based on solving rate equations (RE).

We consider an electromagnetic field consisting of odd harmonics  $\omega_{2q+1}$  of the fundamental radiation with frequency  $\omega_{\text{IR}}$  with phases  $\phi_{2q+1}$  and envelopes  $E_{2q+1}$  characterized by a duration  $\sigma_{2q+1}$ , together with an IR field with phase  $\phi_{\text{IR}}$  and envelope  $E_{\text{IR}}$  characterized by a duration  $\sigma_{\text{IR}}$ :

$$\begin{aligned} \mathbf{E}(t) = & \sum_q \mathbf{E}_{2q+1}[t, \sigma_{2q+1}] \cos(\omega_{2q+1}t + \phi_{2q+1}) + \\ & + \mathbf{E}_{\text{IR}}[(t - \tau), \sigma_{\text{IR}}] \cos(\omega_{\text{IR}}(t - \tau) + \phi_{\text{IR}}). \end{aligned} \quad (4)$$

The temporal shape of the envelopes is assumed to be the same for all XUV harmonics  $E_{2q+1}$ . Their amplitudes are scaled according to the relative strengths shown in Table I. In the RMT calculations, we read in the estimated experimental pulse, sampled on a numerical time grid. In PT and RE, we fitted the pulse to the numerical form and then used  $\sin^2$  envelopes to approximate the gaussians, since this is advantageous for evaluating some of the necessary integrals analytically.

As in the experimental setup, all harmonics are linearly polarized along the quantization axis  $z$  of the atomic system.

#### III.1. R-matrix with Time Dependence (RMT)

RMT is an *ab-initio* technique that solves the time-dependent Schrödinger equation by employing the *R*-matrix paradigm, which divides the configuration space into two separate regions over the radial coordinate of the ejected electron [27]. A general computer code was published [28], with the most recent version available on GitLab [29].

In the inner region, close to the nucleus, the time-dependent *N*-electron wave function is represented by a time-independent *R*-matrix (close-coupling) basis with time-dependent coefficients. In the outer region, the wave function is expressed in terms of residual-ion states coupled with the radial wave function of the ejected electron on a finite-difference grid. The solutions in the two separate regions are then matched directly at their mutual boundary. The wave function is propagated in

the length gauge of the electric dipole operator. For the typical atomic structure descriptions used in RMT, this converges more quickly than the velocity gauge [30]. On the other hand, propagation in the length gauge usually requires more angular momenta to obtain partial-wave-converged results [31, 32].

In the nonrelativistic RMT calculations carried out for the present project, the neon target was described within an  $R$ -matrix inner region of radius 20 (we use atomic units in Sec. III) and an outer region of 15,000. The finite-difference grid spacing in the outer region is 0.08 and the time step for the wave-function propagation was 0.01.

The target was described using the one-electron orbitals generated by Burke and Taylor [33] in their 2-state model, which couples the ionic ground state  $(2s^22p^5)^2P$  and the first excited state  $(2s2p^6)^2S$ . Multiconfiguration expansions, including pseudo-orbitals to account for the term dependence of the physical  $2s$  and  $2p$  orbitals, were employed for both ionic states as well as the initial  $(2s^22p^6)^1S$  state.

We then included all available  $2s^22p^5\epsilon l$  and  $2s2p^6\epsilon l$  channels up to a maximum total orbital angular momentum of  $L_{\max} = 30$ . The continuum functions were constructed from a set of 50  $B$ -splines of order 13 for each angular momentum of the outgoing electron.

In order to extract the transition amplitudes, the final-state radial wavefunction of the ejected electron was projected onto Coulomb functions. This is an improvement over the original formulation of RMT, where the projection was performed onto plane waves, i.e., Bessel functions. While the change had some effect, it did not alter the qualitative nature of the present predictions. Consequently, it seems unlikely that an even more appropriate projection onto distorted Coulomb waves is necessary in light of the other approximations already made in the model.

### III.2. Rate-Equation Approach (RE) and Time-Dependent Perturbation Theory (PT)

Two methods based on the same spectroscopic model were developed: direct numerical solution of a system of rate equations (RE) and non-stationary perturbation theory (PT). Employing two approaches based on the same spectroscopy allows us to clearly distinguish various strong-field effects, such as the Stark shift.

In the RE approach, the wave function of a state is represented as an expansion in a basis of unperturbed atomic wave functions  $\psi_n(\mathbf{r})$ :

$$|\Psi(\mathbf{r}, t)\rangle = \sum_n a_n(t)\psi_n(\mathbf{r}), \quad (5)$$

where the index  $n$  denotes all quantum numbers needed to characterize the state: energy, orbital and total angular momentum, etc. The ‘‘ion+photoelectron’’ states are discretized with an energy step  $\delta\varepsilon = 0.002$ . Substituting Eq. (5) into the Schrödinger equation in

the velocity gauge, one obtains a system of coupled differential equations for the coefficients:

$$\frac{da_n(t)}{dt} = -\frac{i}{c} \sum_i^f e^{i(\varepsilon_n - \varepsilon_i)t} \langle \psi_n | \mathbf{A}(t) \cdot \mathbf{p} | \psi_i \rangle a_i(t). \quad (6)$$

Equation (6) may be solved numerically or serves as the starting point for non-stationary perturbation theory: to begin with, one sets  $a_n^{(0)}(t) = \delta_{n,1}$ , which means that initially the system is in the ground state. Then Eq. (6) is integrated to find the first-order expansion coefficients  $a_n^{(1)}(t)$ . Next, these coefficients are put back into Eq. (6) to obtain the second- and even higher-order approximations. While the sideband oscillations observed in this study are determined by the interference of second-order amplitudes, oscillations in the main line arise due to the interference of first- and third-order amplitudes.

The dipole transition discrete-discrete and discrete-continuum matrix elements were obtained in the  $jK$ -coupling scheme by employing Zatsarinny’s  $B$ -spline  $R$ -matrix (BSR) code [34], which can be run in electron-ion collision mode with appropriately modified boundary conditions. In this coupling scheme, the quantum numbers characterizing a state are the total electronic angular momentum  $J_f$  of the ionic core  $(2p^5)^2P_{J_f}$ , the orbital angular momentum  $l$  of the electron in the discrete  $nl$  or continuum  $\varepsilon l$  part of the spectrum, the intermediate quantum number  $K$  being the result of the vector addition  $\mathbf{K} = \mathbf{J}_f + \mathbf{l}$ , and, finally, the total electronic angular momentum of the system  $\mathbf{J} = \mathbf{K} + \mathbf{1}/2$ , where  $1/2$  is the electron spin. The choice of the  $jK$ -scheme made it possible to carefully take into account transitions from discrete to continuum states with different values of the final ionic  $J_f$  (split by 0.1 eV) in the low-energy region of the spectrum.

The same spectroscopic model as in [35] was used: all possible terms of configurations  $1s^22s^22p^5ns$  ( $n = 3 - 6$ ),  $1s^22s^22p^5nd$  ( $n = 3 - 5$ ),  $1s^22s^22p^43s3p$ ,  $1s^22s^22p^43p4s$ , and  $1s^22s^12p^53s3d$  were included, and the experimental ionization energies [36] were used.

The calculation of the continuum-continuum transition matrix elements was carried out under the assumption that any correlations between the photoelectron and electrons of the residual ion can be neglected. After the self-consistent wave function of the  $(2p^5)^2P$  ion was found with the MCHF software package [37], the wave functions of the continuum electron in the frozen field of this ion were produced. Then, using the method described in [38], the continuum-continuum radial matrix elements  $R_{\varepsilon l, \varepsilon' l'}$  were calculated. The relationship between  $R_{\varepsilon l, \varepsilon' l'}$  and the reduced matrix elements in the  $jK$ -coupling scheme can be obtained using standard formulas from the quantum theory of angular momentum [39].

The results for the  $d$ - to  $f$ -wave transitions coincide with Gordon’s formula [40] to an accuracy of 2 – 3 percent. Being very asymmetric, these transitions proceed mainly by photon absorption and provide the essential contribution to the low-energy part of the spectrum.



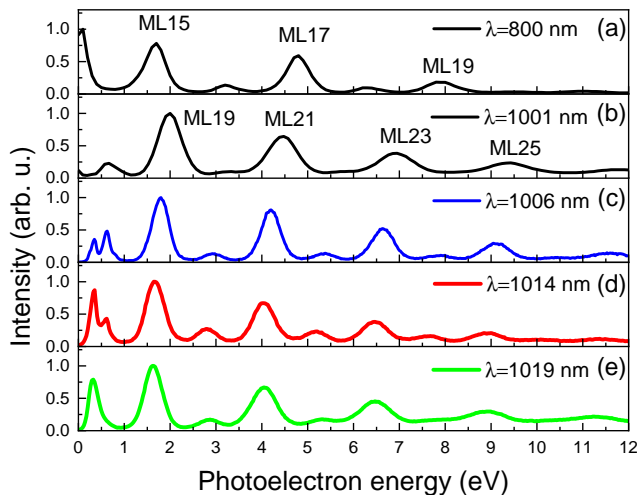


FIG. 2. RABBIT spectra integrated over the IR-XUV delay and acquired for different wavelengths of the driving laser:  $\lambda = 800$  nm (a), 1001 nm (b), 1006 nm (c), 1014 nm (d), and 1019 nm (e). The UT-RABBIT sideband between 0 and 1 eV for the driving wavelengths in the range 1001 – 1019 nm exhibits large variations, as seen in panels (b)-(e). Note in particular the double-peak structure in panels (c) and (d), which is due to near-resonant excitation of at least two states (see text for details). The uncertainty in the estimation of the driving wavelength is about  $\pm 5$  nm.

## IV. RESULTS AND DISCUSSION

### IV.1. Delay-averaged data

Photoelectron spectra acquired with driving laser fields centered at  $\lambda = 800$  nm and  $\lambda$  comprised between 1001 nm and 1019 nm are presented in Fig. 2.

The lowest energy sideband for the 800 nm wavelength is located around the ionization threshold extending up to about 0.2 eV in the continuum. Its signal is stronger than that of the adjacent main line ML<sub>15</sub>. This observation suggests that the sideband is mostly populated through a resonant pathway from below the ionization threshold with the absorption of a photon of the 13<sup>th</sup> harmonic. Comparison with the tabulated data [36] strongly suggests that the resonant state is the  $(2p^5 3d)^1P$ , which can be populated by single-photon absorption from the ground state.

The assignment of the intermediate resonance(s) is more complex in the second range of wavelengths ( $1001 \text{ nm} \leq \lambda \leq 1019 \text{ nm}$ ), as the 17<sup>th</sup> harmonic can reach a spectral region close to the ionization threshold, which is characterized by a high density of bound states. As mentioned previously, the central wavelength around 1010 nm can be slightly tuned by changing the gas pressure in the HCF. This offers the possibility of tuning the energy of the harmonic comb as shown by the four photoelectron spectra presented in panels (b)-(e) of Fig. 2. Interestingly, the characteristics of the first sideband are strongly affected by the precise central wavelength of the driving field. The sideband is

characterized by a single (panels (b) and (e)) or a double (panels (c) and (d)) peak, depending on the specific wavelength. This structure suggests that at least two intermediate bound states are involved in the population of the sideband.

For the detailed investigation of the effects close to the ionization threshold, photoelectron spectra for a central wavelength of  $\lambda \approx 1006$  nm were chosen, with special emphasis on optimizing the spectrometer resolution in the region of low kinetic energies.

In order to identify the largest contributions from the excited resonances involved in the below-threshold ionization pathway, we carried out a series of calculations within the PT model (specifically, we only “switched on” one of the considered intermediate states and omitted all continuum-continuum transitions). The calculated oscillator strengths for selected transitions between the ground and excited states are presented in Fig. 3(a). The largest contributions are presented in Fig. 3(b), together with the contribution due to absorption of one photon of the 19<sup>th</sup> harmonic and the subsequent emission of an IR photon from ML<sub>19</sub>.

The positions of the experimental maxima are in good agreement with the values expected due to ionization from the excited  $(2p^5 4d)^1P$  state. More precisely, although not resolvable in the experiment, from  $2p^5(^2P_{3/2})4d[3/2]$  and  $2p^5(^2P_{1/2})4d[3/2]$  as well as from  $2p^5(^2P_{3/2})5d[3/2]$  and  $2p^5(^2P_{3/2})5d[1/2]$  states to the final ionic states with total electronic angular momentum  $J_f = 1/2$  and  $J_f = 3/2$ , which appear to contribute the most to the formation of SB<sub>18</sub>. The small splitting actually merges the peaks due to the fact that each excited state “prefers” ionization to a specific final ionic state. For instance, ionization of the  $2p^5(^2P_{3/2})4d[3/2]$  (20.7 eV) state leads to  $J_f = 3/2$  in the final ion, while ionization of the  $2p^5(^2P_{1/2})4d[3/2]$  (20.8 eV) state produces  $J_f = 1/2$ . Consequently, the resulting peaks in the spectrum center at the same energy. This fact somewhat justifies employing the nonrelativistic RMT model, which does not take into account the splitting.

The pathways leading to excitation of the intermediate  $2p^5 5s$  and  $2p^5 6s$  resonances are found to play only a secondary role (see white bars in Fig. 3(a)). This is (i) consistent with the propensity rule that the absorption of an XUV photon should preferably excite a state with increased orbital angular momentum [41, 42] and (ii) ionization cross sections from  $d$ -states to an  $f$ -wave ( $d \rightarrow f$ ) are by an order of magnitude larger than the  $s \rightarrow p$  and  $d \rightarrow p$  cross sections near the threshold.

The result of the presence of the two resonances is that the shape of the photoelectron spectrum corresponding to the UT-RABBIT line (SB<sub>18</sub>) strongly depends on the precise driving wavelength, as shown in Fig. 3(c). We can clearly observe a transition from a structure characterized by a single peak centered at high energies ( $\lambda = 1004$  nm; purple, dash-dotted line), to a double peak structure ( $\lambda = 1006$  nm; black, solid line), and finally to a larger peak at lower energies ( $\lambda = 1008$  nm; orange, dashed line). This evolution reproduces the

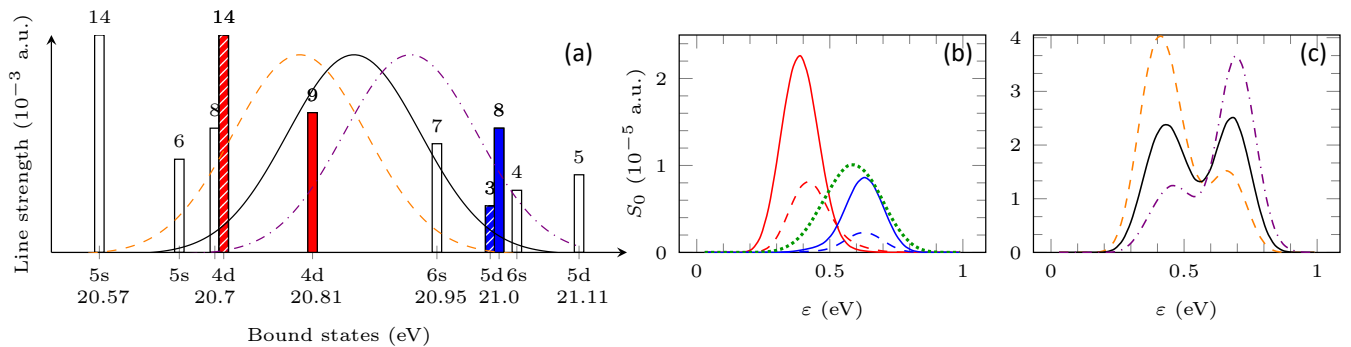


FIG. 3. (a) Energy position of the bound states reached by single-photon excitation starting from the ground state of neon with a driving wavelength of 1006 nm (black gaussian curve), 1008 nm (orange dashed curve), and 1004 nm (purple dash-dotted). The numbers above the columns correspond to the oscillator strength from the ground state. (b) Largest contributions to  $SB_{18}$  in PT from discrete states for a driving wavelength of 1006 nm. The solid red and blue lines correspond to the red ( $2p^5(^2P_{1/2})4d[3/2]$ ) and blue ( $2p^5(^2P_{3/2})5d[3/2]$ ) full columns in panel (a) while the red and blue dashed lines correspond to the red ( $2p^5(^2P_{3/2})4d[3/2]$ ) and blue ( $2p^5(^2P_{3/2})5d[1/2]$ ) hatched columns. The leading uncolored components of the 4d and 5d states are  $2p^5(^2P_{3/2})4d[1/2]$  and  $2p^5(^2P_{1/2})5d[3/2]$ , respectively. The dotted green curve represents the contribution due to absorption of one photon of the 19<sup>th</sup> harmonic and subsequent emission of an IR photon from ML<sub>19</sub>. (c) Delay-averaged near-threshold spectra for 1006 nm (black), 1008 nm (orange dashed) and 1004 nm (purple dash-dotted) as obtained in the PT model.

experimental data presented in Fig. 2, panels (b)-(e).

For the same driving IR field wavelength of 1006 nm, the delay-averaged spectrum and the angular anisotropy parameters  $\beta_2$  and  $\beta_4$  were then extracted. They are presented in Fig. 4 together with the values calculated by the three methods described above. The experimental data for the spectra were scaled to provide a good visual fit to the theoretical predictions. All theoretical curves were shifted to match the central energy position of the first main line (ML<sub>19</sub>) in order to compensate for the Stark shift and make the comparison transparent. Note that the predicted Stark shift is different in the various models (zero in PT, 0.05 eV in RE, and 0.08 eV in RMT). The RMT prediction of the largest value for the Stark shift indicates stronger coupling to the discrete part of the spectrum compared to the other theories.

For electrons with energy above 1 eV (panel (b) of Fig. 4), all theoretical spectra are in a good agreement. In the near-threshold region (panel (a)), however, significant differences are seen due to the role of the discrete states involved in the process. All models exhibit a doublet structure. As discussed above, this doublet originates primarily from the  $2p^54d$  and  $2p^55d$  discrete states acting as intermediate steps in the two-color photoionization process. However, the detailed energy dependence of the doublet is different in each model. Specifically, the RE predictions are closest to the experimental data shown in this panel, while PT exhibits a structure closer to the one seen in Fig. 2(c) for 1006 nm and RMT is closer to the one for 1001 nm (cf. Fig. 2(b)).

The principal reasons for the apparent discrepancy in the shape of the UT-RABBIT peak between the experimental data shown in Fig. 2(c) and Fig. 4(a) are the uncertainty in the determination of the central wavelength and the different distribution of the spectrum of the driving pulse, as well as a possible different IR

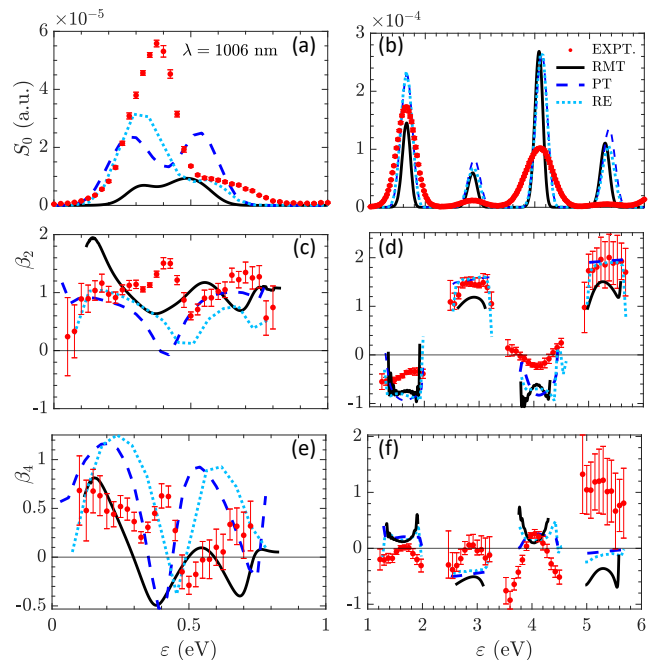


FIG. 4. Parameters for the delay-averaged photoelectron emission at an IR wavelength of 1006 nm: (a,b): spectrum; (c,d): anisotropy parameter  $\beta_2$ ; (e,f): anisotropy parameter  $\beta_4$ . The panels on the left column show the near-threshold region on an extended scale. The red points with error bars represent the experimental data, while the curves correspond to the theoretical predictions from RMT (solid black line), PT (blue dashed line), and RE (blue dotted line). In the gaps on the energy axis in panels (d) and (f), the signal is too low for a meaningful extraction of the parameters. The experimental data for the spectra were scaled to provide a good visual fit to the theoretical predictions.

intensity.

The delay-integrated values of  $\beta_2$  and  $\beta_4$  defined according to Eq. (2) are shown together with the predictions of the various theoretical models in panels (c)-(f) of Fig. 4.

For the AT-RABBIT lines SB<sub>20</sub> and SB<sub>22</sub>, there is good agreement in the retrieved  $\beta_2$  from the experimental data and all theories (see panel (d)). It is also remarkable that all theories show a significant difference between the calculated  $\beta_2$  for the main lines ML<sub>19</sub> and ML<sub>21</sub> and the experimental values. Moreover, within the error bars, the latter are much closer to the single-photon values of  $\beta_2 = -0.5$  for ML<sub>19</sub> and  $-0.16$  for ML<sub>21</sub> [43]. This suggests that the IR intensity, and hence the contribution from third-order terms to the modulation in the main lines, may have been overestimated in the modelling.

In general, the agreement is not very good for  $\beta_4$  (panels (e) and (f)). We note, however, that the determination of  $\beta_4$  is less reliable, since its extraction from the experimental data is more challenging than that of  $\beta_2$ .

For the UT-RABBIT sideband SB<sub>18</sub> (panel (c)), the extracted parameters vary significantly through the line, because several discrete states affect the results to different extent. Note that a resonance often appears in the angular anisotropy parameters in a different way and possibly even at a slightly different energy than for the integrated spectrum [44]. For the line-integrated anisotropy parameters, we found  $\beta_2 = 1.2$  (expt.),  $\beta_2 = 0.9$  (RMT),  $\beta_2 = 0.7$  (RE), and  $\beta_2 = 0.6$  (PT).

All models predict a strong energy dependence in both  $\beta_2$  and  $\beta_4$  across the line in the low-energy region 0.2–0.8 eV. While significant structure is also seen in the experimental data, the details are clearly different. Recall that contributions from photoelectron wave packets initially created via the  $2p^54d$  and  $2p^55d$  intermediate states overlap in this energy range. Together with the need to average the experimental data over windows of energies and space to extract the  $\beta_n$  parameters, this makes reliable calculations extremely challenging and a comparison with experiment difficult.

## IV.2. Delay-resolved data

We now focus the discussion on the comparison of the experimental and calculated data for the first sideband above the ionization threshold (UT-RABBIT). RABBIT traces as a function of the delay  $\tau$  between the XUV and IR fields in the low kinetic energy region are shown for  $\lambda = 800$  nm and  $\lambda = 1006$  nm in Fig. 5(a) and (b), respectively. The intensity oscillations of the first two sidebands can be fitted by cosine functions (see Fig. 5(c,d)), from which the RABBIT phases can be extracted according to Eq. (3). The phase difference between the UT-RABBIT sideband and the first AT-RABBIT sideband is remarkably larger for the 800 nm wavelength driver ( $\Delta\phi = 2.39 \pm 0.13$  rad) compared to the 1006 nm case ( $\Delta\phi = -0.64 \pm 0.27$  rad).

Figures 6 and 7 present comparison of  $S_0$ ,  $S_2$  and  $\phi$  extracted from the experimental data and the simulations. Starting with Fig. 6, we notice good qualitative agreement between all three theories in  $S_0$  for the energy range 1–7 eV (panel (b)), while there are differences near threshold (panel (a)). Note that both the theoretical and the experimental data are cross-normalized between the panels with a single normalization factor. The latter was chosen to give a reasonable visual fit to the experimental data. With the present choice, the integrals under the peaks near 3.4 eV and 4.9 eV are about the same in experiment and the three theories, while the theories underestimate the peak near 1.8 eV and overestimate the one near 6.4 eV. At very low energies, PT and RE reproduce at least qualitatively the fall-off with increasing photoelectron energy, which is due to the peak reaching below ionization threshold. On the other hand, RMT predicts this peak to be further below the threshold than the other two theories. This results in a very small value of  $S_0$  in the 0–1 eV range.

Regarding  $S_2$ , there is better overall agreement among the three sets of theoretical predictions than for  $S_0$ , with the largest differences occurring in the near-threshold region (panel (c)). In the 1–7 eV range (panel (d)), the theories agree well with each other and, after accounting for the different widths of the peaks, the agreement with the experimental predictions also improved compared to  $S_0$ .

Finally, the experimental RABBIT phase is well reproduced by all theories in the energy range 3-7 eV (panel (f)), for the peaks around 3.4 eV, 4.9 eV, and 6.4 eV.

The complex phase evolution for the near-threshold

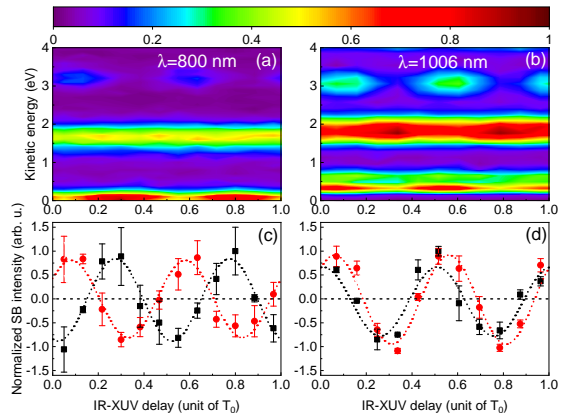


FIG. 5. Top: RABBIT traces for photoelectron energies in the range 0–4 eV for (a) 800 nm and (b) 1006 nm. Bottom: Variation of the sideband signal as a function of the relative delay between the IR and XUV fields, obtained by integrating over an energy window of  $\approx 0.3$  eV for the lowest energy AT-RABBIT sideband (red circles) and the UT-RABBIT sideband (black squares) peaks at (c) 800 nm and (d) 1006 nm. The dotted lines are sinusoidal fits to the experimental data. The oscillations of the sideband signals are plotted relative to the average intensity of the sideband, which we set as the zero line for the normalized intensity.

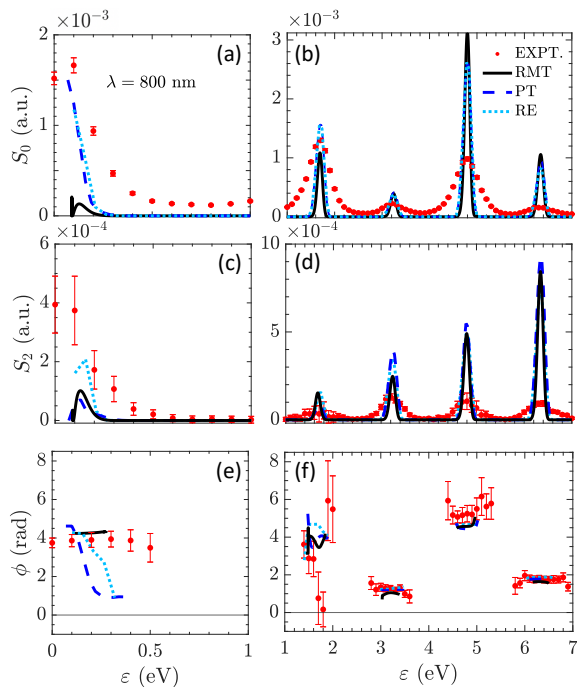


FIG. 6. Delay-averaged parameters for photoelectron emission at an IR wavelength of 800 nm. (a,b): spectrum; (c,d): oscillation amplitude; (e,f): the corresponding phase extracted according to Eq. (3). The panels on the left column show the near-threshold region on an extended scale. Since the phase extraction only makes sense near the peaks of the emission spectra, there are some gaps in the energy between the peaks.

UT-RABBIT sideband and the first mainline around 1.8 eV (see Fig. 6(e,f)) indicates the importance of the under-threshold bound states that complicate the situation. Interestingly, while clearly underestimating the height of the UT-RABBIT sideband, RMT gives a flat phase, whereas PT and RE show a rapid decrease in this energy region (panel (e)). All theories predict a nearly flat phase across the 1.8 eV peak, while the experimental data, albeit with large error bars, suggest a rather strong energy dependence.

Figure 7 shows the corresponding results for a central wavelength of  $\approx 1006$  nm. Panels (a) and (b) are the same as in Fig. 4.

In the near-threshold region, all theories predict a doublet structure in  $S_2$  (panel (c)), similar to that seen in  $S_0$  in Fig. 4(a) and Fig. 7(a). Here the RE model is closest to the experimental data regarding the energy dependence. It should be pointed out that the data presented in Figs. 4 and 7 were taken under slightly different experimental conditions than those presented in Fig. 2. For this reason, care should be taken in evaluating the quality of the comparison. Note, in particular, that the height of the experimental sidebands in panel (b) is relatively low, suggesting that the IR intensity in the calculations was significantly higher than in the experiment. This issue is also clearly seen in panel (d), where the agreement between the theories is at a level

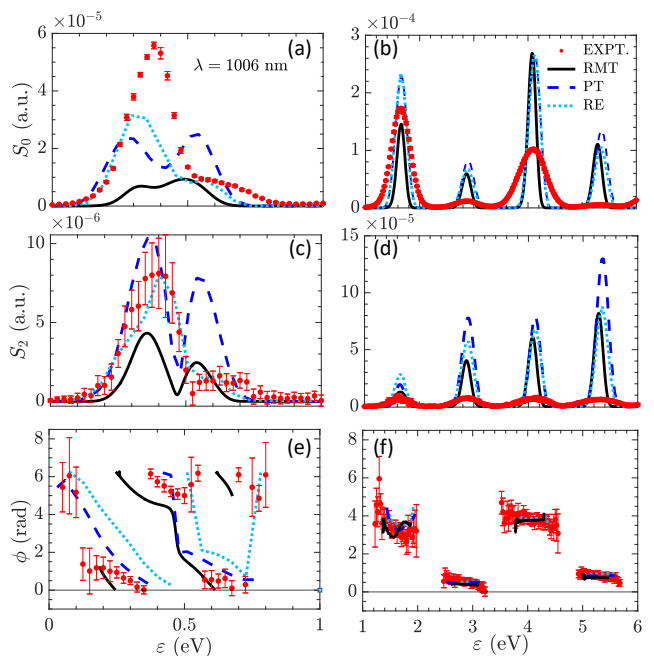


FIG. 7. Delay-averaged parameters for photoelectron emission at an IR wavelength of 1006 nm. (a,b): spectrum; (c,d): oscillation amplitude; (e,f): the corresponding phase extracted according to Eq. (3). The panels on the left column show the near-threshold region on an extended scale. Since the phase extraction only makes sense near the peaks of the emission spectra, there are some gaps in the energy between the peaks.

of about a factor of 2, while the calculated oscillation amplitudes are much larger than in the experimental data.

Looking at the RABBIT phase, we see excellent agreement between all theoretical predictions and also experiment in the 1 – 7 eV region (panel (f)), with a jump of  $\approx \pi$  between consecutive peaks and a nearly constant phase across the peaks. In this case, however, the RABBIT phase varies strongly across the near-threshold structure (panel (e)). The rapid change seen in the experimental data as a function of the ejected-electron energy is to a large extent even quantitatively reproduced by all theories, with RMT being the closest to the experimental data. The principal reason for this rapid variation is, once again, the presence of at least two discrete bound states under the ionization threshold that affect different energy regions of the UT-RABBIT sidebands. The interplay between the contributions of the below-threshold resonances leads to large variations in the phase of the two-color photoionization peak, which are qualitatively reproduced by the theoretical models.

### IV.3. Triple-differential data

In this section we present the energy- and angle-resolved RABBIT phase that we can extract from the experimental and simulated sideband oscillations



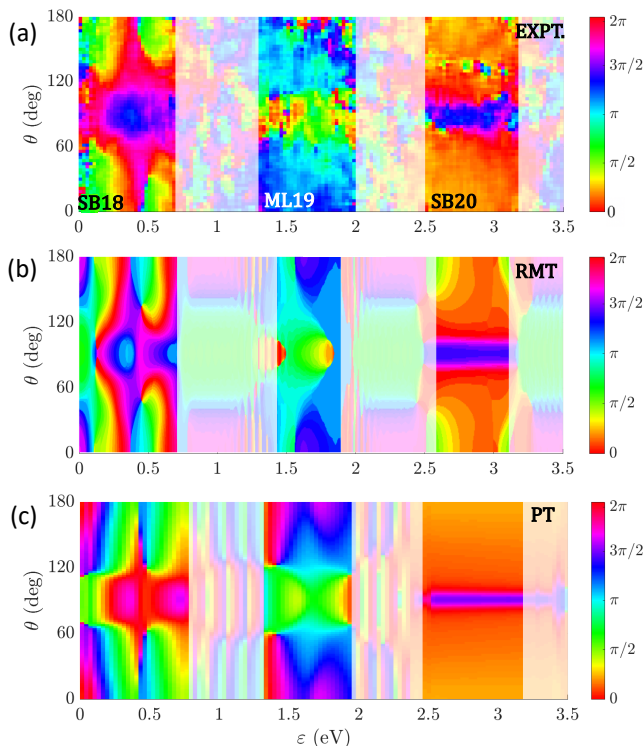


FIG. 8. Angle-resolved atomic phases for the driving field with  $\lambda = 1006$  nm: (a) experiment; (b) RMT; (c) PT. In the energy windows with the faint colors, the signal is too small to allow a meaningful comparison.

according to Eq. (1). As indicated in the discussion of the angle-integrated phases in Figs. 6 and 7, the phase is rather insensitive to details in the peak heights, i.e., the particular IR intensity, as long as one remains in the (second-order) perturbative regime. The evolution of the RABBIT phase  $\phi(\theta)$  over the entire range of angles for the energy interval 0 – 3.5 eV is presented in Fig. 8 for the driving field with  $\lambda = 1006$  nm. Overall, there is very satisfactory agreement between the experimental map and that predicted by the RMT model, especially in light of the fact that SB<sub>18</sub> in the RMT calculation is narrower than in the experiment. The key characteristics of the experimental data are also reproduced by the PT approach. The same is true for the RE map (not shown), which is very similar to that obtained with PT.

The experimental map indicates rapid phase variations around  $\theta = 90^\circ$  as a function of energy. Note that

the cross section here is minimal, since  $\beta_2 > 0$ . This dependence is reproduced well in the calculations. Both the experimental data and the theoretical predictions again exhibit a rich structure in the 0.4 – 0.5 eV energy region, where the pathways through the  $2p^54d$  and  $2p^35d$  resonances provide comparable contributions. The evolution in the proximity of these resonances is well reproduced in the calculations.

## V. CONCLUSIONS

We have presented a joint experimental and theoretical investigation of attosecond photoelectron interferometry around the ionization threshold of neon. Experimental data were acquired using attosecond pulse trains driven by two different driving fields with wavelengths of  $\lambda \approx 800$  nm and  $\lambda \approx 1006$  nm. For the latter configuration, fine-tuning of the driving laser wavelength in the range  $1001 \text{ nm} \leq \lambda \leq 1019 \text{ nm}$  made it possible to change the relative weight of closely-spaced intermediate resonances. The angular-resolved data indicate how the presence of resonances is affecting the photoelectron angular distributions of the sidebands close to the ionization threshold.

## ACKNOWLEDGMENTS

The experimental part of this work was supported by the European Unions Horizon 2020 project 641789 MEDEA. D.B. acknowledges support from the Swedish Research Council grant 2020-06384. G.S. acknowledges support by the Deutsche Forschungsgemeinschaft through Priority Program 1840 (QUTIF) and grant 429805582 (Project SA 3470/4-1). I.M. and G.S. acknowledge support by the BMBF project 05K19VF1, the Deutsche Forschungsgemeinschaft through the Research Training Group DynCAM (RTG 2717), and the Georg H. Endress Foundation. D.E. and G.S. also acknowledge funding by the DFG project International Research Training Group (IRTG) CoCo 2079 and INST 39/1079. The theoretical part of this work was supported by the NSF under OAC-1834740, PHY-2110023, PHY-2408484 (K.B.), OAC-2311928 (K.R.H. and K.B.), the ACCESS allocation PHY-090031, and the Frontera Pathways allocation PHY20028. The RMT calculations were performed on Stampede-2 and Frontera at the Texas Advanced Computing Center.

- 
- [1] P. M. Paul, E. S. Toma, P. Breger, G. Mullot, F. Augé, P. Balcou, H. G. Muller, and P. Agostini, *Science* **292**, 1689 (2001).  
 [2] Y. Mairesse, A. de Bohan, L. J. Frasinski, H. Merdji, L. C. Dinu, P. Monchicourt, P. Breger, M. Kovačev, R. Taïeb, B. Carré, H. G. Muller, P. Agostini, and P. Salières, *Science* **302**, 1540 (2003).  
 [3] K. Varjú, Y. Mairesse, B. Carré, M. B. Gaarde, P. Johnsson, S. Kazamias, R. López-Martens, J. Mauritsson, K. J.

- Schafer, P. H. Balcou, A. L’Huillier, and P. Salières, *Journal of Modern Optics* **52**, 379 (2005).  
 [4] J. M. Dahlström, A. L’Huillier, and A. Maquet, *J. Phys. B: At. Mol. Opt. Phys.* **45**, 183001 (2012).  
 [5] J. M. Dahlström and E. Lindroth, *J. Phys. B: At. Mol. Opt. Phys.* **47**, 124012 (2014).  
 [6] R. Pazourek, S. Nagele, and J. Burgdörfer, *Rev. Mod. Phys.* **87**, 765 (2015).

- [7] D. Bharti, D. Atri-Schuller, G. Menning, K. R. Hamilton, R. Moshhammer, T. Pfeifer, N. Douguet, K. Bartschat, and A. Harth, *Phys. Rev. A* **103**, 022834 (2021).
- [8] D. Bharti, H. Srinivas, F. Shobeiry, K. R. Hamilton, R. Moshhammer, T. Pfeifer, K. Bartschat, and A. Harth, *Phys. Rev. A* **107**, 022801 (2023).
- [9] D. Bharti, H. Srinivas, F. Shobeiry, A. T. Bondy, S. Saha, K. R. Hamilton, R. Moshhammer, T. Pfeifer, K. Bartschat, and A. Harth, *Phys. Rev. A* **109**, 023110 (2024).
- [10] A. S. Kheifets and A. W. Bray, *Phys. Rev. A* **103**, L011101 (2021).
- [11] M. Swoboda, T. Fordell, K. Klünder, J. M. Dahlström, M. Miranda, C. Buth, K. J. Schafer, J. Mauritsson, A. L’Huillier, and M. Gisselbrecht, *Phys. Rev. Lett.* **104**, 103003 (2010).
- [12] A. Autuori, D. Platzter, M. Lejman, G. Gallician, L. Maëder, A. Covolo, L. Bosse, M. Dalui, D. Bresteau, J.-F. Hergott, O. Tcherbakoff, H. J. B. Marroux, V. Lorient, F. Lépine, L. Poisson, R. Taïeb, J. Caillat, and P. Salières, *Science Advances* **8**, eabl7594 (2022).
- [13] L. Drescher, T. Witting, O. Kornilov, and M. J. J. Vrakking, *Phys. Rev. A* **105**, L011101 (2022).
- [14] L. Neoričić, D. Busto, H. Laurell, R. Weissenbilder, M. Ammitzböll, S. Luo, J. Peschel, H. Wikmark, J. Lahl, S. Maclot, R. J. Squibb, S. Zhong, P. Eng-Johnsson, C. L. Arnold, R. Feifel, M. Gisselbrecht, E. Lindroth, and A. L’Huillier, *Frontiers in Physics* **10** (2022), 10.3389/fphy.2022.964586.
- [15] V. Gruson, L. Barreau, A. Jiménez-Galan, F. Risoud, J. Caillat, A. Maquet, B. Carré, F. Lepetit, J. F. Hergott, T. Ruchon, L. Argenti, R. Taïeb, F. Martín, and P. Salières, *Science* **354**, 734 (2016).
- [16] D. M. Villeneuve, P. Hockett, M. J. J. Vrakking, and H. Niikura, *Science* **356**, 1150 (2017).
- [17] P. A. Carpeggiani, E. V. Gryzlova, M. Reduzzi, A. Dubrouil, D. Faccial, M. Negro, K. Ueda, S. M. Burkov, F. Frassetto, F. Stienkemeier, Y. Ovcharenko, M. Meyer, O. Plekan, P. Finetti, K. C. Prince, C. Callegari, A. N. Grum-Grzhimailo, and G. Sansone, *Nature Physics* **15**, 170 (2019).
- [18] E. V. Gryzlova, P. Carpeggiani, M. M. Popova, M. D. Kiselev, N. Douguet, M. Reduzzi, M. Negro, A. Comby, H. Ahmadi, V. Wanie, M. C. Castrovilli, A. Fischer, P. Eng-Johnsson, M. Meyer, K. Bartschat, S. M. Burkov, T. Csizmadia, M. Dumergue, S. Kühn, N. G. Harshitha, M. Fule, F. Aeenehvand, F. Stienkemeier, D. Iablonskyi, K. Ueda, P. Finetti, M. Zangrando, N. Mahne, K. L. Ishikawa, O. Plekan, K. C. Prince, E. Allaria, L. Giannessi, C. Callegari, A. N. Grum-Grzhimailo, and G. Sansone, *Phys. Rev. Res.* **4**, 033231 (2022).
- [19] S. Nandi, E. Plésiat, S. Zhong, A. Palacios, D. Busto, M. Isinger, L. Neoričić, C. L. Arnold, R. J. Squibb, R. Feifel, P. Declava, A. L’Huillier, F. Martín, and M. Gisselbrecht, *Science Advances* **6**, eaba7762 (2020).
- [20] S. Heck, D. Baykusheva, M. Han, J.-B. Ji, C. Perry, X. Gong, and H. J. Wörner, *Sci Adv* **7**, eabj8121 (2021).
- [21] H. Ahmadi, E. Plésiat, M. Moioli, F. Frassetto, L. Poletto, P. Declava, C. D. Schröter, T. Pfeifer, R. Moshhammer, A. Palacios, F. Martín, and G. Sansone, *Nature Communications* **13**, 1242 (2022).
- [22] A. S. Kheifets, *J. Phys. B: At. Mol. Opt. Phys* **56**, 095201 (2023).
- [23] J. Joseph, F. Holzmeier, D. Bresteau, C. Spezzani, T. Ruchon, J. F. Hergott, O. Tcherbakoff, P. D’Oliveira, J. C. Houver, and D. Dowek, *J. Phys. B: At. Mol. Opt. Phys* **53**, 184007 (2020).
- [24] H. Ahmadi, S. Kellerer, D. Ertel, M. Moioli, M. Reduzzi, P. K. Maraju, A. Jäger, R. N. Shah, J. Lutz, F. Frassetto, L. Poletto, F. Bragheri, R. Osellame, T. Pfeifer, C. D. Schröter, R. Moshhammer, and G. Sansone, *Journal of Physics: Photonics* **2**, 024006 (2020).
- [25] D. Ertel, M. Schmoll, S. Kellerer, A. Jäger, R. Weissenbilder, M. Moioli, H. Ahmadi, D. Busto, I. Makos, F. Frassetto, L. Poletto, C. D. Schröter, T. Pfeifer, R. Moshhammer, and G. Sansone, *Review of Scientific Instruments* **94**, 073001 (2023).
- [26] J. Ullrich, R. Moshhammer, A. Dorn, R. Dörner, L. P. H. Schmidt, and H. Schmidt-Böcking, *Rep. Prog. Phys.* **66**, 1463 (2003).
- [27] L. R. Moore, M. A. Lysaght, L. A. A. Nikolopoulos, J. S. Parker, H. W. van der Hart, and K. T. Taylor, *J. Mod. Optics* **58**, 1132 (2011).
- [28] A. C. Brown, G. S. Armstrong, J. Benda, D. D. Clarke, J. Wragg, K. R. Hamilton, Z. Man, J. D. Gorfinkiel, and H. W. van der Hart, *Comp. Phys. Commun.* **250**, 107062 (2020).
- [29] “rmt,” (2023).
- [30] S. Hutchinson, M. A. Lysaght, and H. W. van der Hart, *J. Phys. B: At. Mol. Opt. Phys.* **43**, 095603 (2010).
- [31] E. Cormier and P. Lambropoulos, *J. Phys. B: At. Mol. Opt. Phys.* **29**, 1667 (1996).
- [32] A. N. Grum-Grzhimailo, B. Abeln, K. Bartschat, D. Wefen, and T. Urness, *Phys. Rev. A* **81**, 043408 (2010).
- [33] P. G. Burke and K. T. Taylor, *J. Phys. B: At. Mol. Phys.* **8**, 2620 (1975).
- [34] O. Zatsarinny, *Computer Physics Communications* **174**, 273 (2006).
- [35] M. M. Popova, E. V. Gryzlova, M. D. Kiselev, and A. N. Grum-Grzhimailo, *Symmetry* **13**, 1015 (2021).
- [36] A. Kramida, Y. Ralchenko, J. Reader, and NIST ASD Team, NIST Atomic Spectra Database (ver. 5.11), [Online]. Available: <https://physics.nist.gov/asd> [2024, July 8]. National Institute of Standards and Technology, Gaithersburg, MD. <https://doi.org/10.18434/T4W30F>.
- [37] C. Froese Fischer, T. Brage, and P. Jönsson, *Computational Atomic Structure. An MCHF Approach* (Bristol, Institute of Physics Publishing, 1997).
- [38] T. Mercouris, Y. Komminos, S. Dionissopoulou, and C. A. Nicolaidis, *J. Phys. B: At. Mol. Opt. Phys* **29**, L13 (1996).
- [39] V. V. Balashov, A. N. Grum-Grzhimailo, and N. M. Kabachnik, *Polarization and Correlation Phenomena in Atomic Collisions: A Practical Theory Course* (Kluwer Academic/Plenum Publishers, New York, 2000).
- [40] W. Gordon, *Annalen der Physik* **394**, 1031 (1929).
- [41] U. Fano, *Phys. Rev. A* **32**, 617 (1985).
- [42] D. Busto, J. Vinbladh, S. Zhong, M. Isinger, S. Nandi, S. Maclot, P. Johnsson, M. Gisselbrecht, A. L’Huillier, E. Lindroth, and J. M. Dahlström, *Phys. Rev. Lett.* **123**, 133201 (2019).
- [43] K. Codling, R. G. Houlgate, J. B. West, and P. R. Woodruff, *J. Phys. B: At. Mol. Phys.* **9**, L83 (1976).
- [44] A. N. Grum-Grzhimailo, S. Fritzsche, P. O’Keeffe, and M. Meyer, *J. Phys. B: At. Mol. Opt. Phys* **38**, 2545 (2005).